Supplementary Information:

Structural, optical, and magnetic properties with finite-size and interface effects of noncollinear ferrimagnetic $A\mathrm{Cr_2O_4}$ (A = Ni, Co, Mn) single-domain nanocrystals

Mohamed A. Kassem[1,2,3], Ahmed M. Nashaat[1,2,3], Abdulaziz Abu El-Fadl[2,3]

1. Department of Materials Science and Engineering, Kyoto University, Kyoto 606-8501, Japan
2. *Department of Physics, Faculty of Science, Assiut University, 71516 Assiut, Egypt*
3. *Lab. of Smart Materials for Energy Futures, Faculty of Science, Assiut University, Assiut 71516, Egypt*

S1. Crystal structure of bulk polycrystalline and nanoparticles samples

The powder XRD patterns observed at room temperature for the as-synthesized spinel Ni, Co and Mn chromite nanoparticles and bulk samples (annealed at 1200 °C) are shown with Rietveld refinement results in Fig. S1. Except for the bulk $\mathrm{NiCr_2O_4}$ that crystalizes in a tetragonal structure with a space group $I4_1/amd$ at room temperature, its single-domain nanocrystalline form and the other two spinel cromites in nano and bulk forms crystalize in the cubic $Fd3m$ structure. The inset of Fig. S1(a) demonstrates the splitting of the cubic Ni chromite NCs' (400) peak to tetragonal (004) and (220) peaks after a post annealing at 1200 °C. Table S1 shows the atomic site parameters considered while the XRD pattern analysis for the nano- and bulk spinel chromite $\mathrm{NiCr_2O_4}$. The crystal data and refinement results for the nano- and bulk poly-crystalline spinel Ni, Co and Mn chromites are summarized in Table S2. To investigate the cations distribution between the tetrahedrally A and octahedrally B coordinated sites, we compare the experimentally observed lattice constant to the calculated ones for the cases of normal (δ = 0.0) and partially (with δ = 0.5) and fully (δ = 1.0) inversed spinel structures, assuming a general chemical formula of $(A^{2+}_{1-\delta} \mathrm{Cr}^{4+}_{\delta})[A^{2+}_{\delta} \mathrm{Cr}^{2+}_{\delta} \mathrm{Cr}^{3+}_{2-2\delta}]\mathrm{O_4}$, with the cations in parentheses () and [] locate in the A and B sites, respectively. Figure S2 shows the possible crystal-field splitting schemes of the 3d-levels, and their electronic occupation, for cations available to occupy the A and B sites which are tetrahedrally and octahedrally coordinated by $\mathrm{O^{2-}}$ anions, shown in Fig. S2(a) and (b), respectively. Figure S2(c) shows the experimentally observed and theoretically calculated lattice constants.

Table S1: Atomic site symmetry, occupancy g and site coordinates (*x, y, z*) of ions in the nano- and bulk spinel chromite $NiCr_2O_4$.

Atom	Wyck.	g	x	y	z
Nano (cubic space group $Fd\bar{3}m$, setting #2)					
Ni	8a	1.0	1/8	1/8	1/8
Cr	16d	1.0	1/2	1/2	1/2
O	32e	1.0	$w\ (\approx 0.258)$	w	w
Bulk (tetragonal space group $I4_1/amd$)					
Ni	4b	1.0	0.000	1/4	3/8
Cr	8c	1.0	0.000	0.000	0.000
O	16h	1.0	0.000	$y\ (\approx 0.55)$	$z\ (\approx 0.225)$

Table S2: Crystal structure data and refinement results for the nano- and bulk poly-crystalline spinel Ni, Co and Mn chromites.

Empirical formula	$NiCr_2O_4$		$CoCr_2O_4$		$MnCr_2O_4$	
Sample form	**Nano**	**Bulk**	**Nano**	**Bulk**	**Nano**	**Bulk**
Space group (No.)	$Fd\bar{3}m$ (227)	$I4_1/amd$ (141)	$Fd\bar{3}m$ (227)		$Fd\bar{3}m$ (227)	
Temperature (K)	300		300		300	
Formula mass (g/mol)	226.683		226.923		222.928	
# formula unit per unit cell (Z)	8	4	8		8	
# electrons per unit cell F(000)	864	432	856		840	
Crystallite size (nm)	18(2)	> 100	15(2)	> 100	9(2)	> 100
Calculated density (g/cm³)	5.230	5.235	5.207	5.210	4.921	4.932
Lattice parameters						
a (Å)	8.321(25)	5.833	8.334(3)	8.333	8.443(5)	8.436
b (Å)	8.321(25)	5.833	8.334(3)	8.333	8.443(5)	8.436
c (Å)	8.321(25)	8.452	8.334(3)	8.333	8.443(5)	8.436
$\alpha\ (=\beta=\gamma)\ °$	90	90	90		90	
Unit cell volume (Å³)	575(3)	287(1)	578.9(3)	578(1)	601.8(7)	600.4
Profile function	Pseudo Voigt for bulk and a modified Pseudo Voigt [1] for nano					
Reliability Indices						
Expected R_e (%)	2.558	8.186	2.397	7.386	2.830	6.545
Profile R_p (%)	2.585	8.756	1.953	5.916	2.359	5.081
Weighted profile R_{wp} (%)	3.299	11.612	2.441	7.845	2.960	6.584

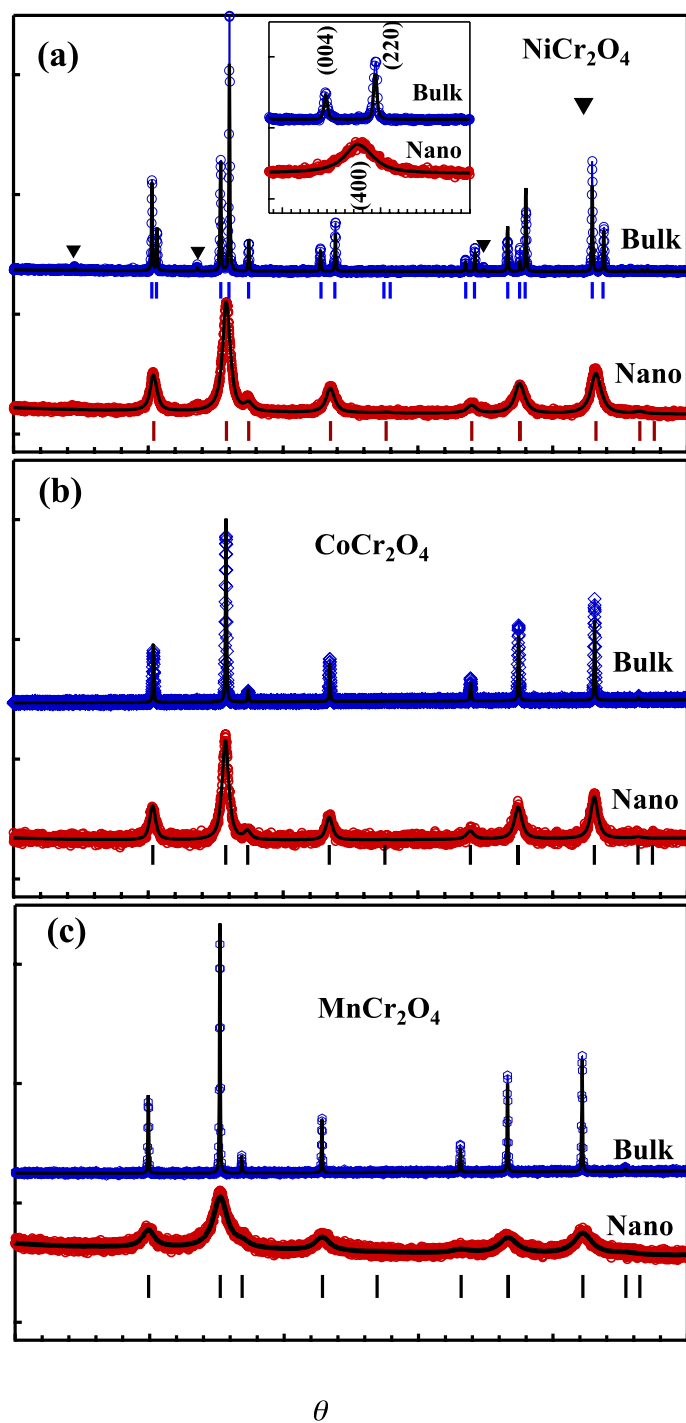| Goodness-of-fit, $S = R_{wp}/R_e$	1.289	1.42	1.0183	1.062	1.0458	1.006

Figure S1: XRD patterns observed at room temperature (marks) shown with Rietveld refinement results (solid lines) of as-synthesized nanoparticles and powder samples annealed at

1200 °C for the Ni, Co and Mn spinel chromites. Vertical bars are the Bragg positions of the spinel chromite phase.
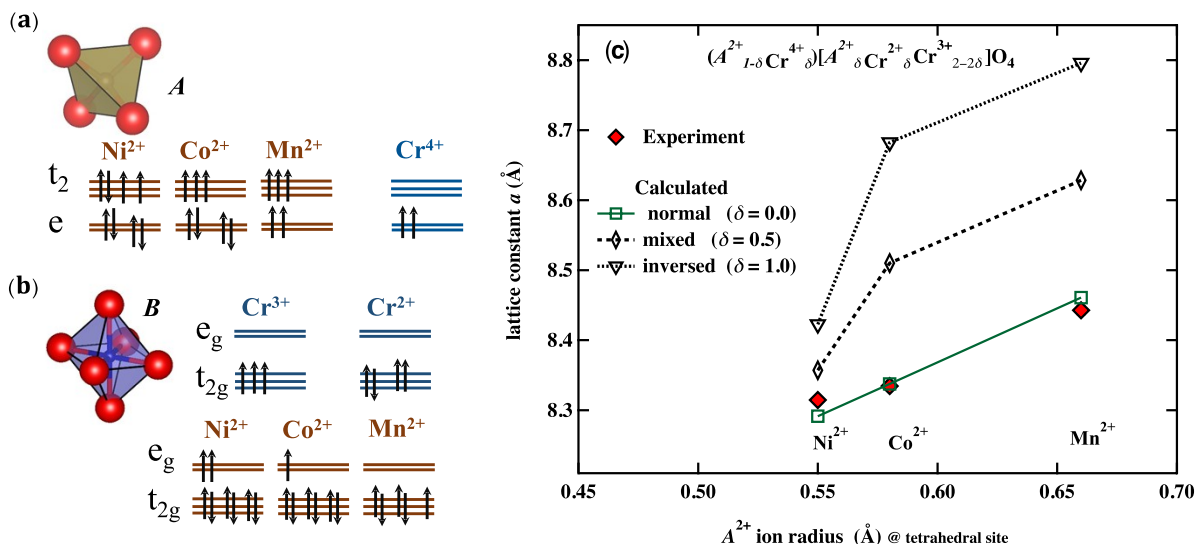

Figure S2: Polyhedra and crystal-field splitting schemes of the 3d-levels, and their electronic occupation, for the available cations in the tetrahedrally A and octahedrally B sites coordinated by O^{2-} anions, shown in (a) and (b), respectively. **(c)** the experimentally observed lattice constant and that is theoretically calculated for the spinel structure $(A^{2+}_{1-\delta}\,Cr^{4+}_{\delta})[A^{2+}_{\delta}\,Cr^{2+}_{\delta}\,Cr^{3+}_{2-2\delta}]O_4$, $A^{2+} = Ni^{2+}$, Co^{2+} and Mn^{2+}, for inversion factor values $\delta = 0.0$, 0.5 and 1.0, plotted as functions of the cation radius of A^{2+} at the tetrahedral site.

S2. TEM and particle size distribution of the nanoparticles

The particle size distribution and average particle size for the as-synthesized nanoparticles of Ni, Co and Mn spinel chromites were estimated via TEM images analyses as described in the main text, section 3.1. Figure S3 shows TEM micrographs for $NiCr_2O_4$, $CoCr_2O_4$ and $MnCr_2O_4$ nanoparticles, with an example of high-resolution TEM images at different magnifications showing the interplanar fringes corresponding indexed planes for the $NiCr_2O_4$ NCs. The particle size histograms were established from the TEM results and fitted using a Lorentzian function.
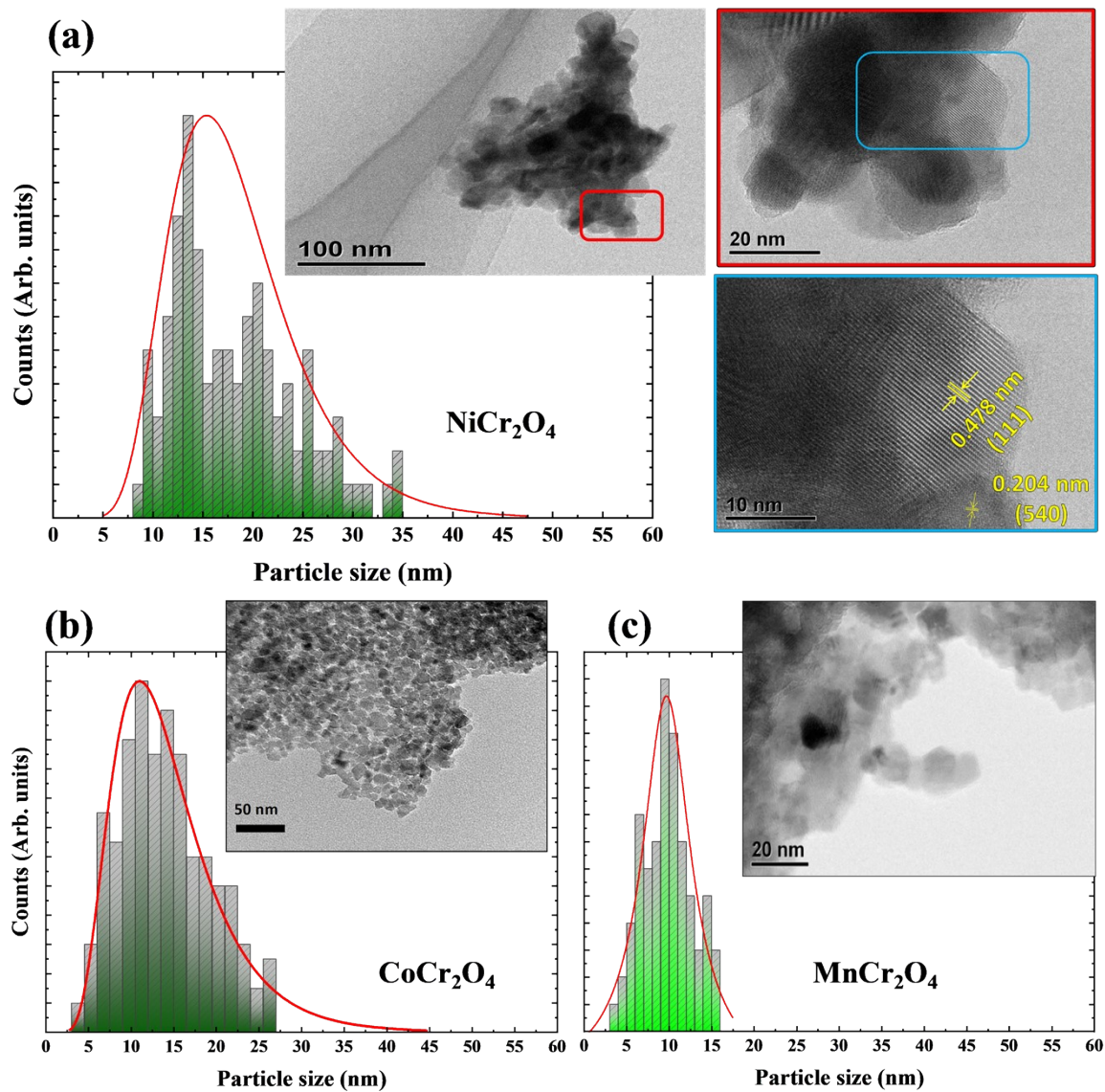
Figure S3. (HR)TEM micrographs for (a) $NiCr_2O_4$ NCs at different magnifications showing the interplanar fringes corresponding the indexed planes, and for (b) $CoCr_2O_4$ and (c) $MnCr_2O_4$ NCs, all with established particle size histograms.

S3. Optical properties of bulk polycrystalline and nanoparticles samples

S3.1. *General features of the optical absorbance*

The optical behavior of both nano and bulk powders is comparatively studied by measuring the optical absorbance of the particles suspended in an aqueous emulsion. As the absorbance behavior is affected by many parameters in this suspension technique, including the homogeneity and the density of the particles suspension, we have optimized the measurement conditions in an energy range of ~ 1 to 5 eV. The absorbance (A) spectra of the compounds in the nano and bulk forms in a wavelength range from 300 to 800 nm are shown in Fig. S4. The absorbance spectra of the as-synthesized nanoparticles, Fig. S4(a), and the bulk powders, Fig. S4(b), demonstrate a common maximum absorption (optical edge) in the UV region of the spectrum. There are additional absorption bands observed in the visible light range (between 550 and 725 nm) which vary in position and intensity for the different compounds and different forms of nano and bulk particles, as seen in Fig. S4(a). Main features are observed for the Co chromite spectra including the shaper absorption edge among the three chromite NCs when compared to its bulk form behavior. A deconvolution of its low-energy absorption asymmetric band indicates two peaks around ~ 620 nm and 665 nm with a slight shift to low energy in the NCs form. The band deconvolution is more distinct for the material in the bulk form with almost same intensity of the two peaks, however, the 665-nm peak becomes much intense in the material's NCs from, as seen in Figs. S4 (b) and (c). In case of the Ni chromite, there is more inclination for the NCs absorbance at the absorption edge when compared to its bulk spectrum, with the development of a small band around ~675 nm in both the nano and bulk spectra without a peak splitting. In the case of $MnCr_2O_4$ the bulk spectrum is almost identical in behavior with the nano form without any observable additional bands below the absorption edge. These absorption bands are attributed to spin-allowed and intra-atomic d-d transitions of the A^{2+} cations as described in section S3.3 below.
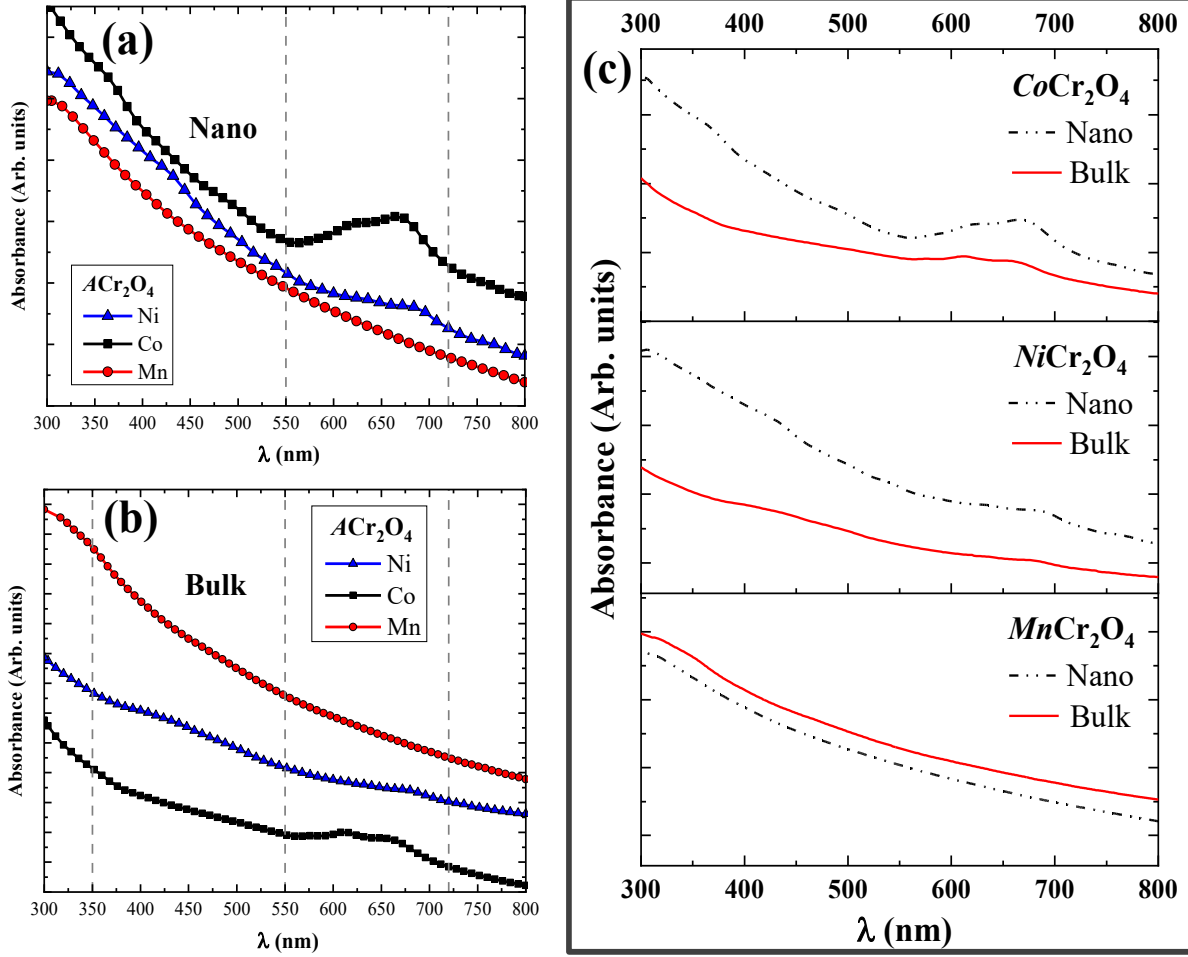
Figure S4. Absorbance spectra of **(a)** as-synthesized nanoparticles and **(b)** bulk post-annealed particles, with small vertical offsets for clarity. **(c)** Comparison of the absorbance behavior of the bulk and nano forms of each compound (spectra are shifted vertically for clarity).

S3.2. *Tauc's plots and the optical energy gap estimation*

The absorption coefficient (α) can be estimated by employing the Beer-Lambert law [2] with considering the theoretical density ρ in gm/cm^3 of the material, as:

$$\alpha = \frac{A\,\rho}{c\,l},$$

(S3-1)

where c is the concentration of the sample in the solvent and l is the distance travelled by the light through the suspension. Corelating α with the incident photon energy $h\upsilon$ gives the general Tauc's expression [3]

$$\alpha h\upsilon = B(h\upsilon - E_g)^n.$$

(S3-2)

Where B is a probability constant, and n is an exponent that determines the transition type. The optical performance of the samples is tested according to the typical allowed direct transition

behavior with $n=1/2$ and with n=2 for the indirect bandgap transition. To investigate the nature of the optical transitions' nature, two plots of $(\alpha h\nu)^2$ *vs h\nu* and $(\alpha h\nu)^{1/2}$ *vs h\nu* were plotted to test the developing of the absorption band for the nano (Fig. S5) and for the bulk (Fig. S6(a)). The development of the absorption edge was found more consistent for the $(\alpha h\nu)^2$ plot which implies the direct bandgap nature, while the indirect curve does not exhibit the band edge clearly. Similar observation was reported by Suchomski et al.,[4] for $CoCr_2O_4$ thin films. We observe, however, that the Tauc's plots demonstrated in Figs. 3(b), S4 – S6 of the allowed direct transitions, the samples do not exhibit the expected sudden increase on the onset of the band edge. This behavior can be assumed due to the broad particle size distribution which contributes to the electronic transition but with an overall dominance of the band gap above 3 eV. The effect of the suspension interaction with the particles and the particle interaction in the suspension can affect the behavior as a suspension of ultrafine particles can give better shape of Tauc's plot as reported for the nanosuspension prepared by laser ablation [5]. A direct bandgap for $CoCr_2O_4$ thin films were reported with similar behavior [6].

The values of E_g were estimated by linear extrapolation of data at high photon energy region, where the optical absorption is stable, to $(\alpha h\nu)^2 = 0$. The estimated values of E_g, presented in Table 2 (in the main text), are consistent with results of optical conductivity investigations for bulk chromites with a direct bandgap of $CoCr_2O_4$ nanoparticles were reported as ~3.1 eV [4,7,8]. The interpretation of the difference between the bulk and nano curves Fig. S6 especially in case of Co and Ni chromites can be attributed to the change of the band structure in the nanoparticles from that in bulk forms. For example, additional defects are expected in the nano form which can result in tails within the bandgap, this is probably the dominant effect at this particle size rather than an expected quantum confinement effect that results in a wider energy gap.

S3.3. *Intra-atomic d–d transition of Co^{2+} and Ni^{2+} ions in tetrahedrally coordinated sites*

Theoretically, based on the ligand field theory by strong-coupling approximation [9–12], there are three spin allowed intra-atomic d–d transitions for Co^{2+} ions in a tetrahedrally site, as the case here of $CoCr_2O_4$, which are ${}^4A_2$ $(e^4t_2^3)\rightarrow$ ${}^4T_1(e^3t_2^4)$, ${}^4A_2$ $(e^4t_2^3)\rightarrow$ ${}^4T_2(e^3t_2^4)$ and ${}^4A_2$ $(e^4t_2^3)\rightarrow$ ${}^4T_1(e^2t_2^5)$. The latter two excitations occur at low photon energies with the ${}^4A_2$ $(e^4t_2^3)\rightarrow$ ${}^4T_1(e^2t_2^5)$ of a rather small oscillator strength to be experimentally observed. The ${}^4A_2$ $(e^4t_2^3)\rightarrow$ ${}^4T_2(e^3t_2^4)$ transition occurs with a transition energy of $\omega = \Delta E$ (~ 0.8 eV) lower than the measurement range [8]. The optical absorption band observed here is assigned to the ${}^4A_2$ $(e^4t_2^3)\rightarrow$ ${}^4T_1(e^3t_2^4)$ excitation with a transition energy of $\omega = \Delta E +12B$, where ΔE is the splitting energy between the e and t_2 orbitals and B is the Racah parameter [8]. The main two intra-atomic d-d transition of Co^{2+} ions in a tetrahedrally site were observed and reported for many compounds such as Cs_3CoCl_5 at 0.9 and 2.0 eV [13], ZnO:Co

at 0.9 and 2.0 eV, ZnS:Co and CdS:Co at 0.8 and 1.8 eV [14]. For chromium spinels were observed in bulk $CoCr_2S_4$ at 0.7 and 1.3 eV [15] and $CoCr_2O_4$ single crystals at 0.8 and 2 eV [8]. The $^4A_2$ ($e^4t_2^3$)$\rightarrow$ $^4T_1(e^3t_2^4)$ transition can split into a dipole-allowed $^4A_{2g} \rightarrow {}^4T_{2u}$ and a dipole-forbidden $^4A_{2g} \rightarrow {}^4T_{1g}$ transitions by the Davydov splitting [16], which explains the asymmetric band with peaks observed at 1.86 and 2 eV. As well as the visible light asymmetric band, we also observed a very small kink around ~370 nm which can be attributed to the additional ligand-metal charge transfer combination with the admissible d-d transitions.

In the case Ni^{2+} ions with d^8 $(e^4t_2^4)$ configuration in a tetrahedrally site, mainly two d-d transitions, $^3T_1$ $(e^4t_2^4) \rightarrow {}^3T_2(e^3t_2^5)$ with a transition energy $\omega = \Delta E - 3B$ and $^3T_1$ $(e^4t_2^4) \rightarrow {}^3T_1(e^3t_2^5)$ with $\omega = \Delta E + 9B$, can occur. Both were observed for a $NiCr_2O_4$ single crystal at 0.94 and 1.95 eV [7]. A weaker broad band is observed here in the absorbance spectrum of $NiCr_2O_4$ with maxima around ~685 nm, which is mainly assigned to the $^3T_1$ $(e^4t_2^4) \rightarrow {}^3T_1(e^3t_2^5)$ of the Ni^{2+} ions with a transition energy $\omega = \Delta E + 9B$ [7]. The broadening of the band developed for $NiCr_2O_4$ spectrum may be attributed to the overlapping of the d-d transitions resulted from the splitting in 3d level of the Ni^{2+} cation as shown in Fig. S4. Also, a small band is observed around ~450 nm, can be attributed to an additional ligand-metal charge transfer combination with the d-d transitions. Similar bands are reported for the Ni^{2+} in the tetrahedral coordination of $NiAl_2O_4$ [17]. At room temperature bulk $NiCr_2O_4$ symmetry is tetragonal but for our nano samples the observed room temperature phase is cubic, which may influence the band structure of the material and may introduce different d-d transitions at different energies. As expected, the intensity of the absorption bands in $NiCr_2O_4$ with Ni^{2+} are lower in intensity of the optical band when compared to $CoCr_2O_4$ nanoparticles. Furthermore, in the case of $NiCr_2O_4$ the spin-orbit interaction may be involved in the analysis of the energy dependence of the compound. The intra-atomic d-d transitions are spin-forbidden between half-filled orbitals in Mn^{2+} ions in the tetrahedrally site with the high-spin d^5 state, which explains the absence of the additional absorption band below the optical edge of $MnCr_2O_4$. Although a d-d transition of the Cr^{3+} ions is possible, with an assigned absorption band observed in unpolarized reflectivity and optical conductivity spectra around 1.6 eV, its oscillator strength is relatively weak [7]. Due to the absence of excitation band below the optical edge in the spectrum of $MnCr_2O_4$, we exclude the contribution of d-d transition of the Cr^{3+} ions in the additional absorption bands observed here for Ni and Co chromites.
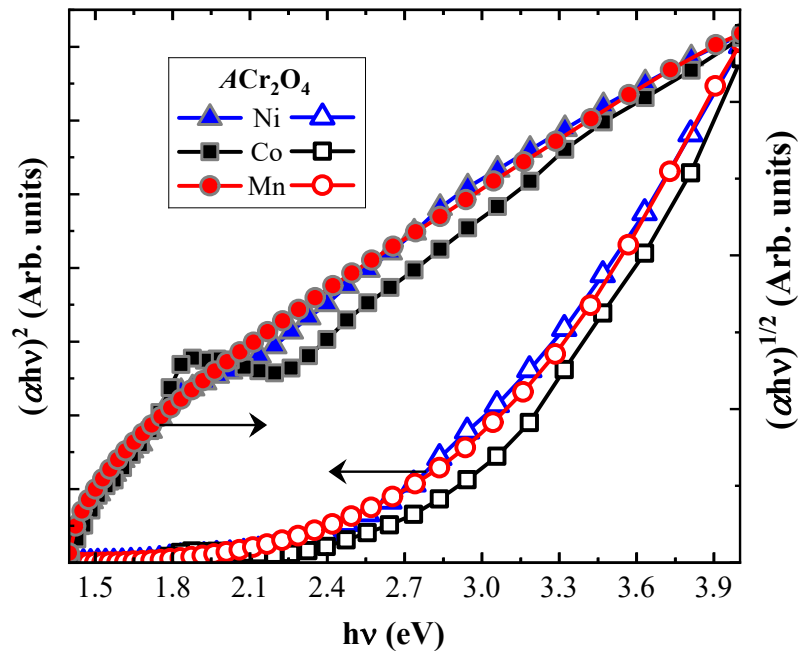
Figure S5. (a) Tauc's plots to check for the allowed direct and indirect transitions for the three compounds as-synthesized nanoparticles.
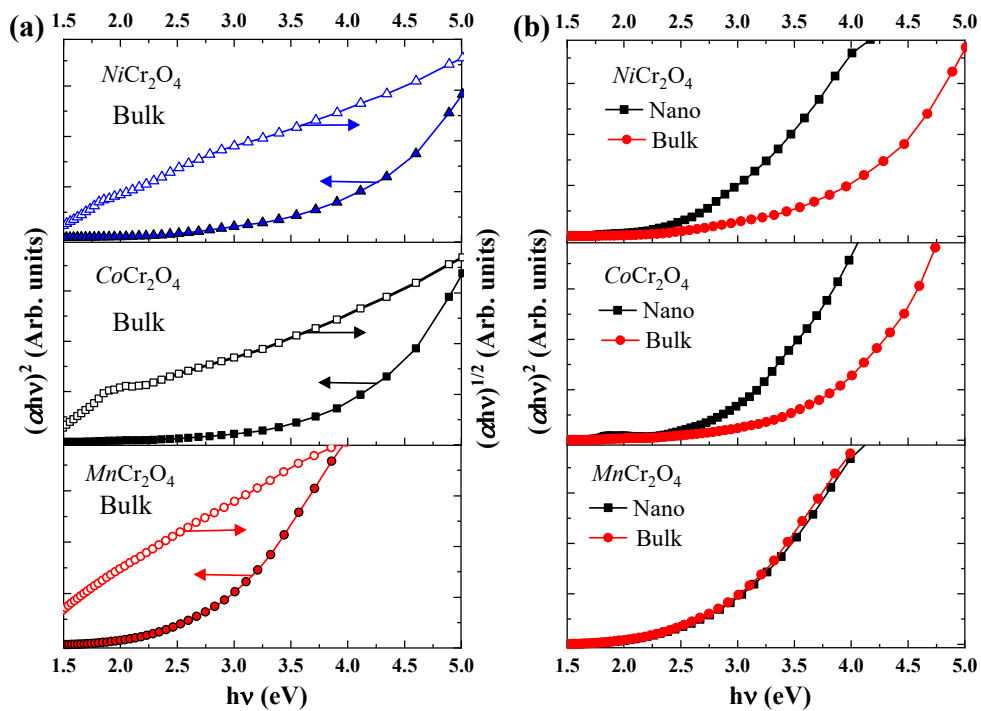

Figure S6. (a) Tauc's plot test for the allowed direct and indirect transitions for the three compounds a bulk form. **(b)** Tauc's plot comparison for the allowed direct transition for the three compounds in bulk and nano forms.

S4. Static magnetization of bulk polycrystalline and nanoparticles samples

Figures S7 show temperature (T) dependence data of the static magnetization (M) of as-synthesized nanoparticles and bulk annealed samples of the spinel Ni, Co, and Mn chromites measured at an applied magnetic field H = 100 Oe after ZFC and FC processes. The data are presented as M/H vs T in Figs. S7(a) - (c) with the low-temperature ZFC data in the insets, and as the difference (M_{FC} - M_{ZFC}) vs T in Figs. S7(d) - (f). The bulk magnetization is about one order of magnitude larger and below the Cutie temperature T_C, anomalies corresponding the bulk noncollinear FIM transition (to canted AFM state in $NiCr_2O_4$, and spiral FIM order in $CoCr_2O_4$ and $MnCr_2O_4$) are observed at T_s = 29 (and 27) , 26 (and 24) and 19 K in both $M(T)/H$ and $M_{FC}(T)$ - $M_{ZFC}(T)$ for the Ni, Co and Mn bulk (and as-synthesized NCs) chromites, respectively. On the other hand, the bulk 'lock-in' transition to a commensurate spiral order in Co and Mn chromites is observed at T_s = 15 and 14 K, respectively, but is suppressed in their nanoparticles with 13 and 10 nm particle sizes, respectively. We can not observe a transition anomaly corresponding to the spiral order in the Mn chromite NCs. The observed magnetic transitions in the bulk chromites agree with the reported magnetization and neutron diffraction results. The magnetic transitions in the NCs form are described in detail in section 3.3.1 in the main text. One notes that the noncollinear FIM transitions at T_s are largely hidden in the ZFC magnetization of the NCs, probably by a dominant surface disorder. However, unlike the bulk behavior, a low-temperature spin freezing is indicated by a blocking peak in the $M_{ZFC}(T)$ at a temperature $T_{f2} \approx$ 13 and 5 K for the Ni and Co Chromite NCs, respectively, these are in addition to the ZFC magnetization peak at T_{f1} just below T_C.

S5. Core-shell magnetic spinel chromite nanoparticles.

We assume that each particle magnetically consists of a bulk magnetic core and a surface disordered shell. Above the Curie temperature T_C, the whole particle exhibits a homogeneous spin disorder in a paramagnetic behavior. With decreasing the temperature below T_C, a magnetic transition to a collinear Néel-type FIM order occurs in the particle's core while a spin disorder due to lack of a spin compensation is maintained in each particle's surface shell, as shown in inset of Fig. 5(i). About 20, 35, and 28% of the nanoparticle's magnetization is a bulk magnetization maintained in its magnetic core, which is surrounded by a magnetically dead layer of an average thickness of ~ 3.4, 1.9 and 1.8 nm for the Ni, Co, and Mn as-synthesized chromite NCs, respectively, as described in the sub-section 3.3.2 in the main text. With a further decrease of temperature below T_s, the core exhibits a noncollinear FIM order with a relatively unstable state below T_s and subsequent additional spin-spin interaction (magnetic exchange) at the core-shell interface and spin-charge (magnetoelectric) interaction within the noncollinear FIM core.
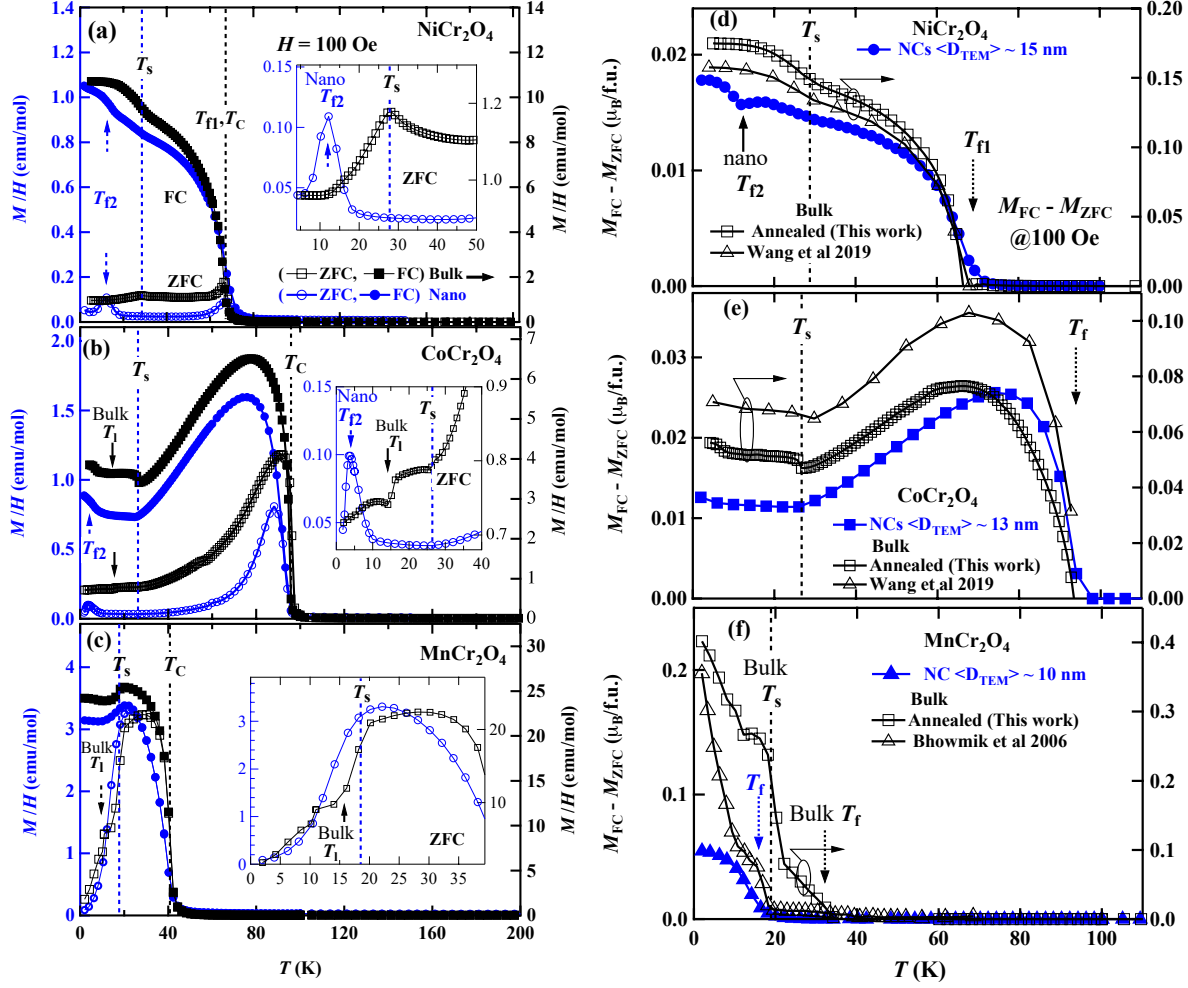
Figure S7: Temperature dependence of the static magnetic susceptibility (M/H) measured at 100 Oe after ZFC (open) and FC (solid) processes; (a), (b), and (c); and of the FC magnetization splitting from ZFC magnetization, M_{FC}-M_{ZFC}, measured at 100 Oe; (d), (e) and (f); for $NiCr_2O_4$, $CoCr_2O_4$ and $MnCr_2O_4$ bulk powder and NCs.
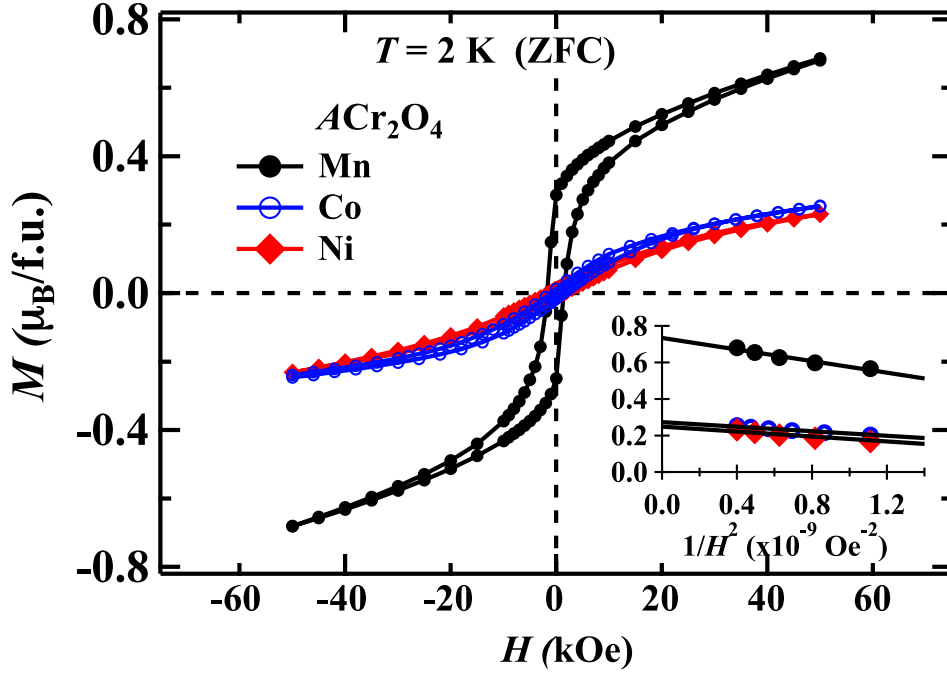
Figure S8: Isothermal magnetic ZFC hysteresis loops $M(H)$ of $NiCr_2O_4$, $CoCr_2O_4$ and $MnCr_2O_4$ NCs measured at 2 K. Inset shows the corresponding $M(H)$ *vs.* $1/H^2$ plots

S6. The single domain critical size

Small magnetic nanoparticles below a certain critical size behave as single domain particles and they do not benefit energetically from the wall formation. Assuming almost spherical particles, we can approximately estimate the single-domain maximum size as [18],

$$D_{SD} \approx \frac{18\sqrt{A\,K_1}}{\mu_0 M_s^2},$$ (S6-1)

with $A \approx \dfrac{3\,k_B T_C}{z\,a}$ is the exchange stiffness and $K_1 \approx \dfrac{H_c\,M_s}{2}$ (at least for the Co chromite with cubic symmetry and <100> easy axes down to low temperatures) is the anisotropy constant, respectively, assuming the Stoner–Wohlfarth model for randomly oriented identical particles[19,20]. Here, M_s is the saturation magnetization in emu/g, k_B is the Boltzmann constant, and z is the effective number of the nearest neighbors, T_C is the Curie temperature and H_c is the coercive field, all in cgs units. Applying these criteria with values of H_c and M_s at 2 K results in critical single-domain sizes of about 110, 200 and 56 nm for the $NiCr_2O_4$, $CoCr_2O_4$ and $MnCr_2O_4$ NCs, respectively. This approximate estimation indicates that our

spinel chromite nanoparticles with particles sizes up to 35, 25 and 15 nm, respectively as shown in in Fig. S3, are single-domain magnetic particles free from domain walls.
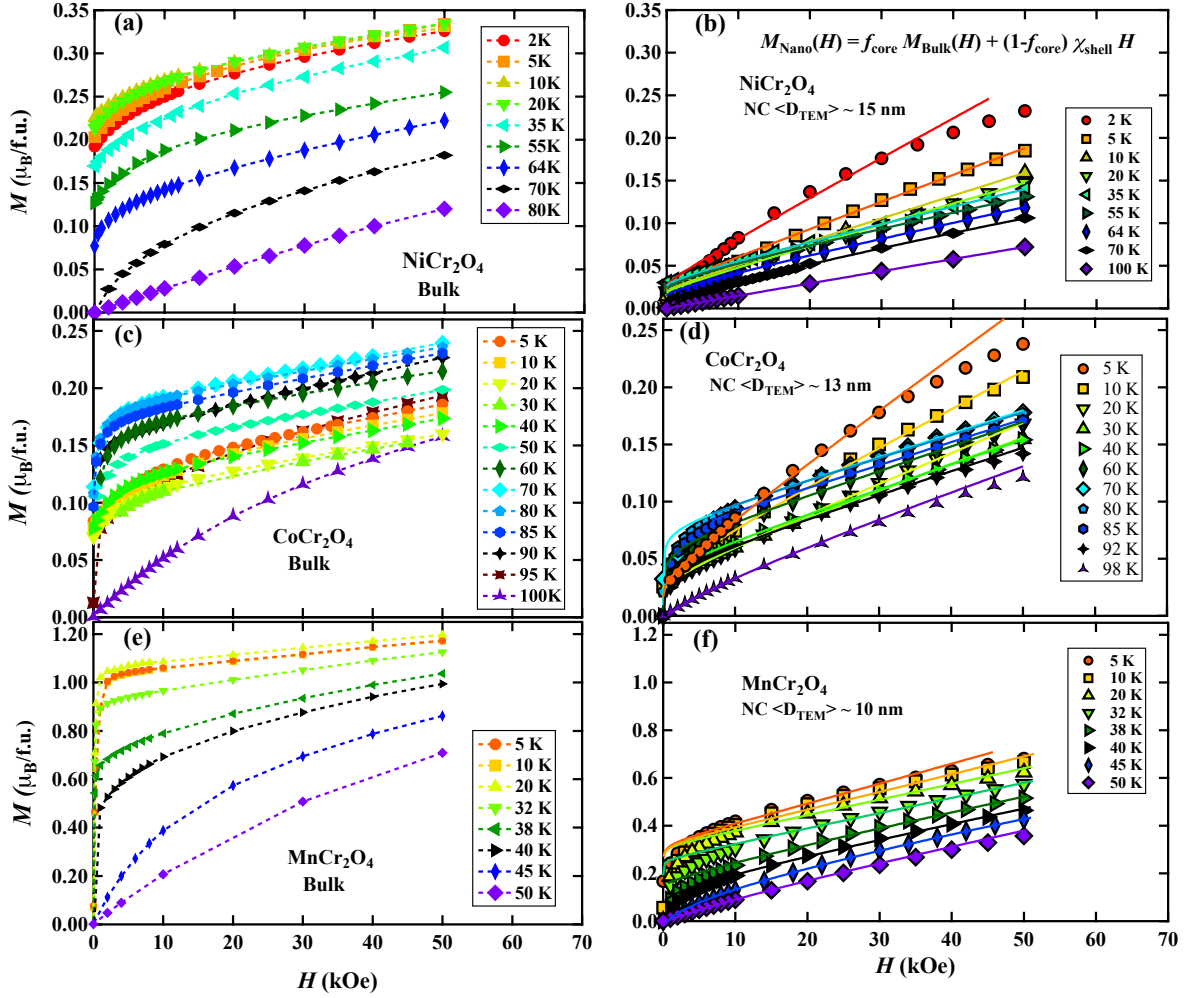

Figure S9. Isothermal initial magnetization curves $M(H)$ measured using annealed bulk samples and as-synthesized nanocrystals for $NiCr_2O_4$ in (a), (b); $CoCr_2O_4$ in (c), (d); and $MnCr_2O_4$ in (e), (f); respectively. Solid lines in (b), (d) and (f) are fits of the nanoparticles experimental data (symbols) to Eq. (7) in main text employing isothermal bulk data in (a), (c) and (e), respectively.
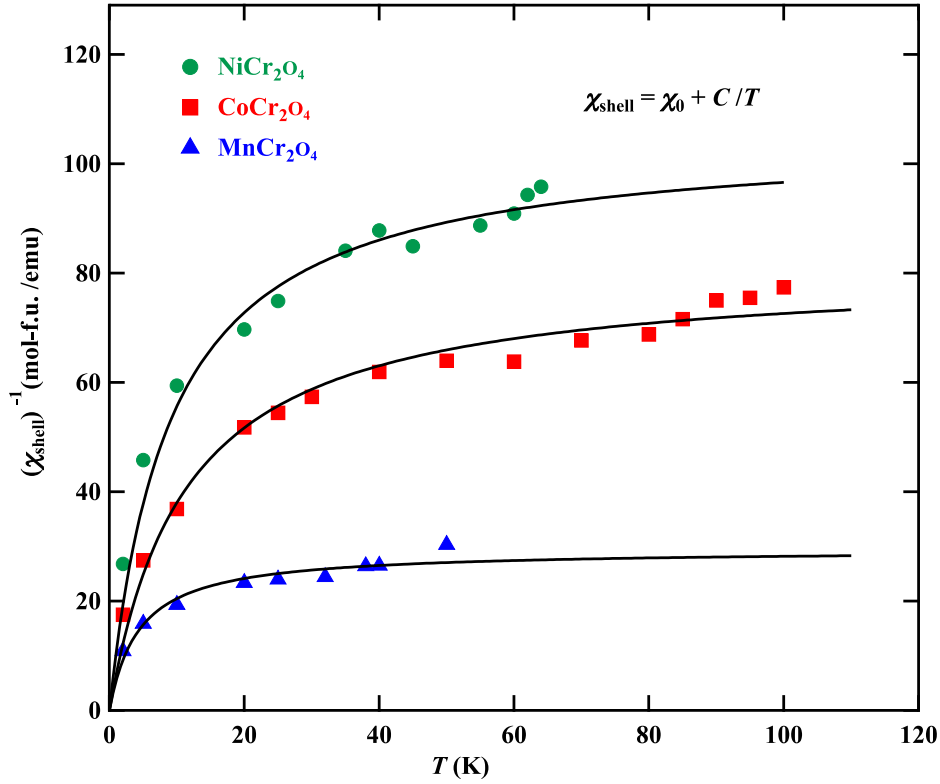
Figure S10. The temperature dependence of the distinguished shell susceptibility of ACr_2O_4 (A= Ni,

$$\chi_{Shell} = \chi_0 + \frac{C}{T}$$

Co, Mn) NCs. Solid lines represent fittings to a modified Curie law

References:

[1]   F. Izumi, T. Ikeda, A rietveld-analysis programm RIETAN-98 and its applications to zeolites, in: Materials Science Forum, Trans Tech Publ, 2000: pp. 198–205.
[2]   D.F. Swinehart, The beer-lambert law, J Chem Educ 39 (1962) 333.
[3]   J. Tauc, Optical properties and electronic structure of amorphous Ge and Si, Mater Res Bull (1968). https://doi.org/10.1016/0025-5408(68)90023-8.
[4]   C. Suchomski, C. Reitz, K. Brezesinski, C. Tavares De Sousa, M. Rohnke, K.I. Iimura, J.P. Esteves De Araujo, T. Brezesinski, Structural, optical, and magnetic properties of highly ordered mesoporous MCr 2O 4 and MCr 2- xFe xO 4 (M = Co, Zn) spinel thin films with uniform 15 nm diameter pores and tunable nanocrystalline domain sizes, Chemistry of Materials 24 (2012) 155–165. https://doi.org/10.1021/CM2026043.
[5]   J.H. Ryu, G.S. Park, K.M. Kim, C.S. Lim, J.W. Yoon, K.B. Shim, Synthesis of CaWO4 nanocolloidal suspension via pulsed laser ablation and its optical properties, Appl Phys A Mater Sci Process 88 (2007). https://doi.org/10.1007/s00339-007-4051-4.
[6]   C. Suchomski, C. Reitz, K. Brezesinski, C. Tavares de Sousa, M. Rohnke, K. Iimura, J.P. Esteves de Araujo, T. Brezesinski, Structural, Optical, and Magnetic Properties of Highly Ordered Mesoporous MCr2O4 and MCr2–x Fe x O4 (M= Co, Zn) Spinel Thin Films with Uniform 15 nm Diameter Pores and Tunable Nanocrystalline Domain Sizes, Chemistry of Materials 24 (2012) 155–165.

[7]   V. Kocsis, S. Bordács, D. Varjas, K. Penc, A. Abouelsayed, C.A. Kuntscher, K. Ohgushi, Y. Tokura, I. Kézsmárki, Magnetoelasticity in ACr2O4 spinel oxides (A= Mn, Fe, Co, Ni, and Cu), Phys Rev B Condens Matter Mater Phys 87 (2013) 064416. https://doi.org/10.1103/PHYSREVB.87.064416/FIGURES/11/MEDIUM.

[8]   K. Ohgushi, Y. Okimoto, T. Ogasawara, S. Miyasaka, Y. Tokura, Magnetic, Optical, and Magnetooptical Properties of Spinel-Type A Cr 2 X 4 (A =Mn, Fe, Co, Cu, Zn, Cd; X =O, S, Se), J. Phys. Soc. Jpn. 77 (2008) 034713. https://doi.org/10.1143/JPSJ.77.034713.

[9]   R.G. Burns, Mineralogical applications of crystal field theory. Second edition, Mineralogical Applications of Crystal Field Theory. Second Edition (1993).

[10]   C.K. Jørgensen, Absorption spectra and chemical bonding in complexes, Elsevier, 2015.

[11]   H. Kamimura, S. Sugano, Y. Tanabe, Ligand field theory and its applications, Syokabo, Tokyo 224 (1969).

[12]   J.S. Griffith, L.D. Roberts, The Theory of the Transition-Metal Ions , Phys Today 15 (1962). https://doi.org/10.1063/1.3057810.

[13]   J. Ferguson, Crystal spectra of metal coordination compounds. I. Tetrahedral cobalt(II), J Chem Phys 32 (1960). https://doi.org/10.1063/1.1730729.

[14]   H.A. Weakliem, Optical spectra of Ni2+, Co2+, and Cu2+ in tetrahedral sites in crystals, J Chem Phys 36 (1962). https://doi.org/10.1063/1.1732840.

[15]   R.K. Ahrenkiel, T.H. Lee, S.L. Lyu, F. Moser, Giant magneto-reflectance of CoCr2S4, Solid State Commun 12 (1973). https://doi.org/10.1016/0038-1098(73)90124-5.

[16]   A.S. Davydov, Theory of Molecular Excitons, 1971. https://doi.org/10.1007/978-1-4899-5169-4.

[17]   M. Ulrich, J. García-Otero, J. Rivas, A. Bunde, Slow relaxation in ferromagnetic nanoparticles: Indication of spin-glass behavior, Phys Rev B Condens Matter Mater Phys 67 (2003).

[18]   J.M.D. Coey, Magnetism and Magnetic Materials, Cambridge University Press, 2010. https://doi.org/10.1016/0160-9327(88)90178-0.

[19]   N.A. Usov, S.E. Peschany, Theoretical hysteresis loops for single-domain particles with cubic anisotropy, J Magn Magn Mater 174 (1997) 247–260. https://doi.org/10.1016/S0304-8853(97)00180-7.

[20]   E.C. Stoner, E. Wohlfarth, A mechanism of magnetic hysteresis in heterogeneous alloys, . . Phil. Trans. R. Soc. Lond A 240 (1948) 599–642.